THE JOURNAL OF PHYSICAL CHEMISTRY Letters

Letter

Cite This: J. Phys. Chem. Lett. 2019, 10, 2400−2407

pubs.acs.org/JPCL

Millimeter-Sized Single-Crystal $CsPbrB_3$/CuI Heterojunction for High-Performance Self-Powered Photodetector

Yong Zhang, Siyuan Li, Wei Yang, Mahesh Kumar Joshi, and Xiaosheng Fang*

Department of Materials Science, Fudan University, Shanghai, 200433, P.R. China

Supporting Information

ABSTRACT: Millimeter-sized $CsPbBr_3$ single crystals were prepared via a facile solvent-evaporation method in ambient environment. The heterojunction between p-type CuI and n-type $CsPbBr_3$ was formed by a simple immersion process. The as-integrated $CsPbBr_3$/CuI device exhibits a good rectifying behavior (ratio of 250 at ±2 V). In particular, the photodetector shows excellent self-powered characteristics under 540 nm light illumination, including high photocurrent (near 100 nA); high photosensitivity (on/off ratio of 1.5×10^3); fast response speed (0.04/2.96 ms); and good wavelength selectivity (565−525 nm), responsivity (1.4 mA W^{-1}), and detectivity (6.2×10^{10} Jones). This work provides a simple, low-cost, and effective method for preparing millimeter-level $CsPbBr_3$ single crystals. The simple device architecture further provides a promising approach for fabricating high-performance self-powered photodetectors.

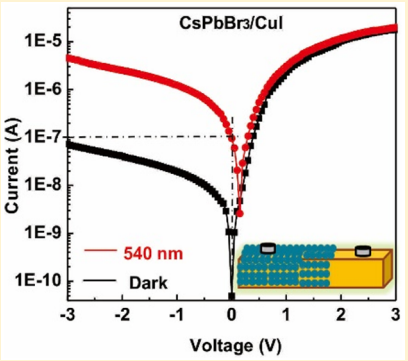

Recently, metal halide perovskites have attracted growing attention in the field of optoelectronics because of their remarkable optical and electronic properties, including tunable direct band gap, high electron mobility, long electron−hole diffusion length, simple processing technique, and facile integration with various semiconductor materials.[1−8] These unique features allow such perovskite materials to be promising candidates for various optoelectronic devices, such as photovoltaics, luminescent devices, and photodetectors.[9−12] Particularly, photodetectors (PDs), as one of the most significant optoelectronic devices that can directly transform light illumination into an electrical signal, show a wide range of applications such as machine vision, surveillance, and imaging.[13−16] It is noteworthy to mention that the organic−inorganic hybrid perovskites are unstable and degenerate rapidly when they are exposed to air or heat. Among the various perovskites, $CsPbBr_3$, an inorganic perovskite, exhibits many advantages, such as a remarkable stability besides the superior features inherited from the hybrid perovskite structure, thereby drawing great attention in the field of photodetection.[17,18] The micrometer-level $CsPbBr_3$ crystals can be prepared by chemical vapor deposition.[19] Moreover, $CsPbBr_3$ single crystals with a well-defined structure possess a clear cutting band edge, reduced trap densities, and high carrier diffusion lengths, resulting in high-performance photodetectors.[20−22] Therefore, the preparation of large-size $CsPbBr_3$ single crystals is urgent for high-performance photodetectors.

Large-size perovskite crystals are critical for both fundamental properties and efficient photodetection. The $CsPbBr_3$ single crystals were usually prepared through a variety of solution-based methods, such as inversion temperature crystallization, antisolvent vapor-assisted crystallization, and seeded solution crystal growth,[22−25] which rely on high temperature, complex processes, and vacuum. Recently, Yang et al. developed a low-temperature, space-limited, and substrate-independent growth technique for millimeter-sized $CsPbBr_3$ monocrystalline films, which presents excellent stability and high photodetection performance.[26] Saidaminov et al. presented a rapid low-temperature and solution-based synthesis of millimeter-level $CsPbBr_3$ single crystals, and the device showed self-powered behavior with a high on/off ratio by sandwiching $CsPbBr_3$ between Au and Pt contacts.[27] These experiments still require complex experimental processes and external tools. Therefore, preparing large-size $CsPbBr_3$ single crystals via a simple and low-cost method is still in demand. Meanwhile, many composite photodetectors based on $CsPbBr_3$ (quantum dots, nanosheets, and polycrystalline films) such as $CsPbBr_3$/ZnO and $CsPbBr_3$/TiO_2 have been reported with enhanced performance.[28−32] However, the fabrication of composite devices based on large-size $CsPbBr_3$ single crystals is rarely noticed, and it is still worth researching to boost device performance and develop integrated features.

In recent years, copper-based compounds (CuO, CuS, CuI, and CuSCN) have attracted significant attention because of simple preparation technology and special physicochemical properties.[33−35] Owing to point defects (copper vacancies) in the crystals, these materials typically exhibit excellent p-type conductivities. Among them, CuI has a direct wide band gap of 3.1 eV, a high exciton binding energy (62 meV), a high hole mobility, a low resistivity, and the advantages of simple preparation and low cost. Thus, it has wide variety of applications in the field of optoelectronic devices, such as

Received: April 4, 2019
Accepted: April 24, 2019
Published: April 24, 2019

DOI: 10.1021/acs.jpclett.9b00960
J. Phys. Chem. Lett. 2019, 10, 2400−2407

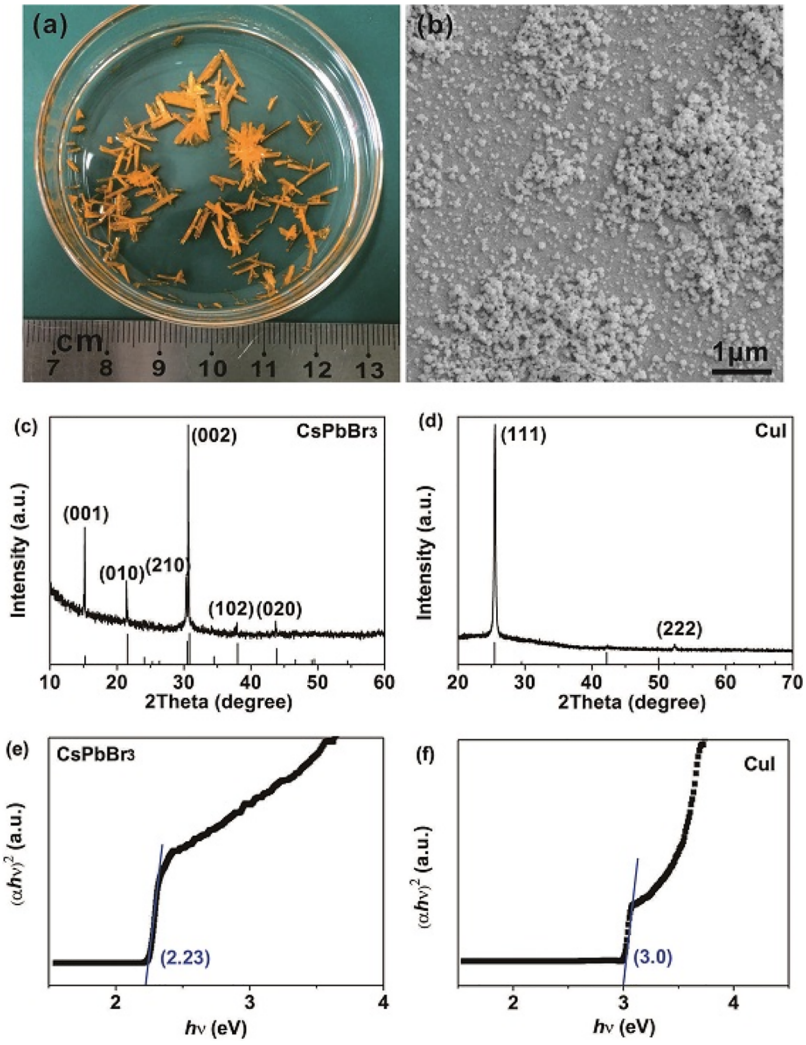

Figure 1. (a) Digital image of $CsPbBr_3$ crystals and (b) SEM image of CuI particles. XRD patterns of (c) $CsPbBr_3$ crystals and (d) CuI particles. Tauc plots of (e) $CsPbBr_3$ crystals and (f) CuI particles obtained from their absorbance spectra.

light-emitting diodes, field effect transistors, and dye-sensitized solar cells.[36−38] Yang et al. have reported bipolar diodes based on an epitaxial thin-film heterojunction of p-CuI/n-ZnO with a high rectification of 2×10^9 (±2 V) and a low saturation current density of 5×10^{-9} A cm^{-2}.[39] CuI is usually used as a hole injection layer and can be directly contacted with other semiconductor materials, while $CsPbBr_3$ has balanced electron−hole diffusion lengths and a high absorption coefficient over the visible region. However, there is very limited work on photodetectors based on $CsPbBr_3$/CuI, and exploring the device feasibility and special properties is worthwhile.

In this work, we synthesized millimeter-level $CsPbBr_3$ single crystals by a simple solution processing technique at a low temperature in ambient environment. The $CsPbBr_3$/CuI heterojunction was formed by a facile immersion and heating process. The as-fabricated $CsPbBr_3$/CuI device was examined to determine its photoelectric performances. It was found that the device demonstrates a good photodiode behavior. More importantly, the $CsPbBr_3$/CuI photodetector exhibits excellent self-powered characteristics at 540 nm light illumination. In addition, both $CsPbBr_3$ and $CsPbBr_3$/CuI devices present high performance at −3 V at 540 nm light illumination. This work provides a facile and low-cost method to fabricate high-performance, self-powered photodetectors based on $CsPbBr_3$ single crystals.

Millimeter-sized $CsPbBr_3$ single crystals were synthesized by direct evaporation of an equimolar $CsBr/PbBr_2$ solution (prepared in dimethyl sulfoxide) at a low temperature (40 °C) in ambient environment. A small amount of aqueous HI solution was added to promote crystal growth prior to the solvent evaporation. As shown in Figure 1a, the yellow $CsPbBr_3$ single crystals were obtained with the prolongation of heating time. Most crystals are cuboid in shape, ranging in length from 4 to 10 mm, with an average length of 6 mm and the longest length of up to 1.5 cm (Figure S1a). Some small $CsPbBr_3$ crystals are self-assembled into a big flower-like crystal. The crumbly $CsPbBr_3$ crystals were carefully cleaned and employed to construct devices. The fabrication of an individual $CsPbBr_3$/CuI heterojunction was achieved by dipping a part of a long $CsPbBr_3$ crystal into CuI acetonitrile solution for 1 min followed by heating at 60 °C for 10 min. The as-prepared millimeter-sized $CsPbBr_3$ single crystals provide a promising platform to integrate with other semiconductor materials for various devices. Figures 1b and S1b display the scanning electron microscopy (SEM) images of the CuI particles with different magnifications. The results show that the CuI particles are spheroidal with the diameter

DOI: 10.1021/acs.jpclett.9b00960
J. Phys. Chem. Lett. 2019, 10, 2400−2407

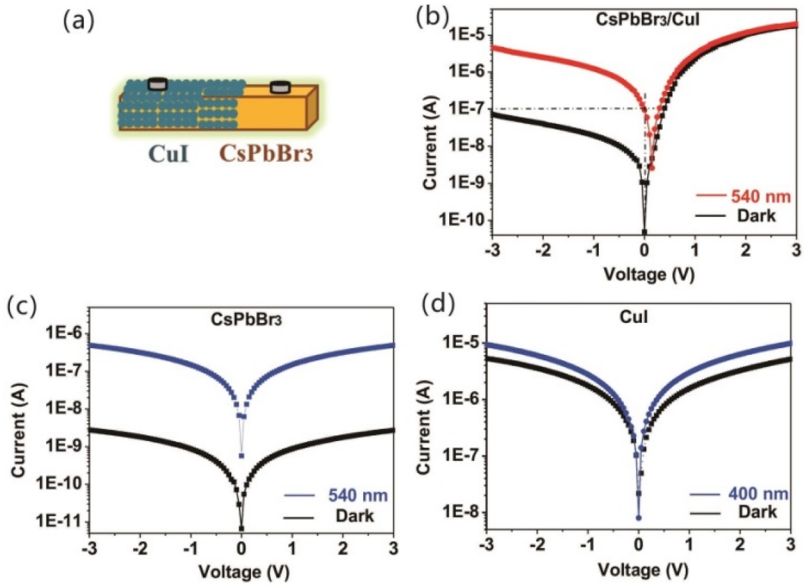

Figure 2. (a) Schematic illustration of the device structure. *I*−*V* characteristics of different devices in the dark and under 540 nm light illumination: (b) $CsPbBr_3$/CuI heterojunction PD, (c) single $CsPbBr_3$ crystal PD, and (d) pure CuI PD.

ranging from 50 to 150 nm. Moreover, some particles are aggregated together to form agglomerates, and a few nanoplates are also formed, as shown in Figure S1b. The $CsPbBr_3$ crystals and CuI nanoparticles are all prepared by a facile cost-effective method. Panels c and d of Figure 1 demonstrate the X-ray diffraction (XRD) patterns of the $CsPbBr_3$ crystals and the CuI particles, respectively. As shown in Figure 1c, the diffraction peaks for the $CsPbBr_3$ single crystal appearing at 15.2°, 21.5°, 30.5°, 30.8°, 38.0°, and 43.8° are assigned to (001), (010), (210), (002), (102), and (020) crystal planes of monoclinic cesium lead bromide (JCPDF No. 54-0571), respectively. All the peak positions of the $CsPbBr_3$ and their relative intensities are in good agreement with the lattice parameters of a = 9.843 Å, b = 4.127 Å, and c = 6.874 Å, confirming the phase of the as-obtained sample. The line widths of all the peaks are very small, which implies that the $CsPbBr_3$ crystals are well-prepared with a high crystalline quality. The distinct peak at 2θ of 30.8° corresponds to the (002) crystal plane of $CsPbBr_3$, indicating that the crystal exposed face is the (002) plane. As seen in Figure 1d, the strong and sharp peak located at 25.5° and the very weak peak located at 52.3° are indexed to the (111) and (222) planes of cubic CuI (JCPDF No. 06-0246), respectively. All these results suggest that the as-obtained $CsPbBr_3$ crystals and CuI particles possess good crystallinity.

Furthermore, X-ray photoelectron spectroscopy (XPS) patterns were employed to analyze the surface chemical components and the states of the different elements in $CsPbBr_3$ crystals. The full survey spectrum of the $CsPbBr_3$ sample (Figure S2a) reveals the dominant existence of Cs, Pb, and Br elements. The binding energy peak located at 725.6 eV is related to Cs $3d_{5/2}$ (Figure S2b), and the splitting peaks located at 140.5 and 145.3 eV can be assigned to Pb $4f_{7/2}$ and Pb $4f_{5/2}$ (Figure S2c), respectively. The binding energy peak located at 70.5 eV can be ascribed to Br $3d_{5/2}$ (Figure S 2d), confirming the existence of Br in $CsPbBr_3$ samples. Signals from other impurities was not noticed in $CsPbBr_3$, also demonstrating the high purity of the samples, which are in accordance with the XRD results. In addition, the UV−vis absorption spectra of $CsPbBr_3$ crystals and CuI particles were measured to study their optical properties. As shown in Figure S3a,b, the sharp absorption edges of $CsPbBr_3$ and CuI are at around 540 and 410 nm, respectively, revealing the highly crystalline characteristic of the samples. The optical band gap could be estimated by the Tauc plots using the UV−vis absorbance spectroscopy. The $CsPbBr_3$ and the CuI are direct band gap semiconductors. As shown in Figure 1e,f, the band gaps of as-prepared $CsPbBr_3$ crystals and CuI particles are estimated to be 2.23 and 3.0 eV, respectively, both of which are close to the theoretical values. The simplicity of our method will permit promising use of millimeter-sized $CsPbBr_3$ single crystals for in-depth fundamental studies and a wide range of practical applications.

To enhance the optoelectronic performance of a large-size $CsPbBr_3$ single crystal device and explore its self-powered characteristics, CuI was integrated with $CsPbBr_3$ single crystals. Figure 2a shows the schematic illustration of the photodetectors based on an individual $CsPbBr_3$/CuI composite. Part of the cuboid $CsPbBr_3$ single crystal was covered with a CuI particle film to form a heterojunction, and the device was manually fabricated by using silver paste with a small area as the electrodes. The photoelectric properties of $CsPbBr_3$/CuI devices were carefully studied using a two-probe method at room temperature. Figure 2b demonstrates the typical current−voltage (*I*−*V*) curves of the individual $CsPbBr_3$/CuI heterojunction in a logarithmic plot in the dark and upon 540 nm light illumination. The dark current of the $CsPbBr_3$/CuI device exhibits an on-state at the forward bias and an off-state at the reverse bias, which indicates the successful formation of heterojunction and reveals a typical photodiode behavior. The photodiode shows a high rectification ratio of 250 at ±2 V, similar to the transparent p-CuI/n-ZnO diode reported by Yang et al.[39] The photocurrent could reach 4.5 μA under 540 nm light illumination (power density of 1.276 mW cm^{-2}), which is much higher than the dark current under the reverse bias and slightly lower than the forward bias. More importantly, the remarkable difference between the dark-current and photocurrent at zero bias demonstrates the

DOI: 10.1021/acs.jpclett.9b00960
J. Phys. Chem. Lett. 2019, 10, 2400−2407

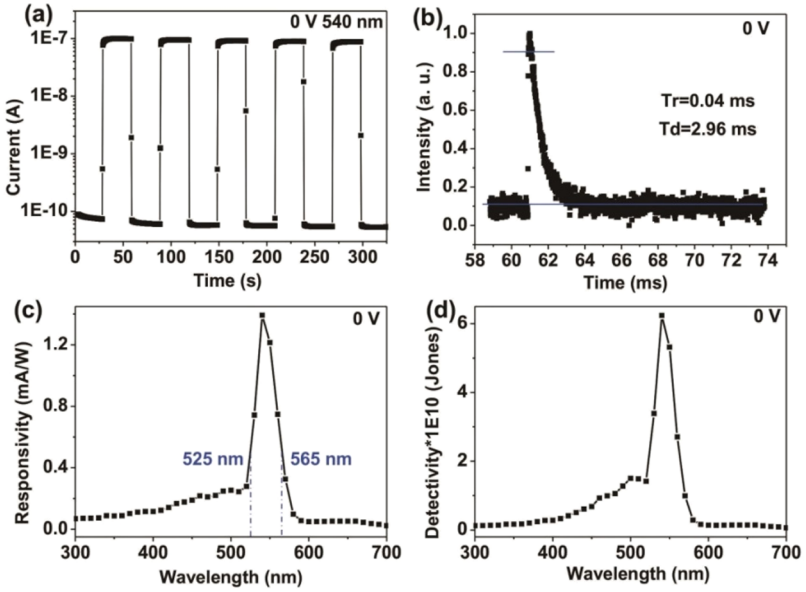

Figure 3. (a) $I-t$ characteristics of $CsPbBr_3$/CuI PD under dark conditions and at 540 nm light illumination. (b) Corresponding pulse response under 10 Hz 355 nm pulse laser radiation. (c) Spectral responsivity and (d) detectivity characteristics of the $CsPbBr_3$/CuI PD with irradiance wavelength ranging from 700 to 300 nm under 0 V bias.

excellent self-powered behavior of the $CsPbBr_3$/CuI device. As shown in Figure 2c,d, the $I-V$ curves of the pure $CsPbBr_3$ and CuI devices under dark conditions and light illumination show symmetrical features, which indicate that the Schottky junction between the silver electrodes and $CsPbBr_3$ is negligible, unable to induce a self-powered behavior. These results demonstrate that the self-powered behavior of the $CsPbBr_3$/CuI device mainly originates from the heterojunction between $CsPbBr_3$ and CuI, and the device exhibits typical photodiode characteristics. The device exhibits the photovoltaic effect under 540 nm light illumination at zero bias, which provides an open-circuit voltage of 0.15 V and a short-circuit current of nearly 100 nA. The large difference between photocurrent and dark current of the $CsPbBr_3$ device indicates that it has an excellent photoresponse at 540 nm light. The $I-V$ curves of the CuI device show slightly higher photocurrent at 400 nm light than that of the dark current. These results indicate that the as-fabricated $CsPbBr_3$/CuI device can work without an external power supply and is a photovoltaic detector, because the built-in electric field can act as the driving force to separate the electron-hole pairs and produce a large photocurrent. CuI is a p-type inorganic semiconductor with a high hole mobility and is usually used as hole transport layer in the field of solar cells. $CsPbBr_3$ crystal has a high carrier mobility with balanced electron−hole diffusion lengths over the visible region and can act as an n-type inorganic semiconductor. Therefore, the as-prepared n-$CsPbBr_3$/p-CuI device exhibits good rectifying characteristics and an excellent self-powered feature.

The reproducibility and speed of photoresponse are key parameters in the characterization of photodetectors. Figure 3a exhibits the photocurrent (I_{ph}) response curves based on the $CsPbBr_3$/CuI device irradiated with 540 nm light at zero bias. The current−time ($I-t$) characteristics demonstrate rapid photoresponse and good reproducibility without noticeable photocurrent decay of the device. The photocurrent of the device increases rapidly to a steady state and then decreases quickly when the light is switched on and off without external power supply. This indicates a rapid separation of electron−hole pairs by the built-in electric field near the heterojunction. The photocurrent of the device can reach up to 100 nA at zero bias under 540 nm light illumination. The photosensitivity (defined as the ratio of photocurrent to dark current, I_{ph}/I_d) of the device is calculated to be 1.5×10^3. Furthermore, the accurate response time of the $CsPbBr_3$/CuI device under zero voltage bias was recorded by a photoresponse measurement system, as shown in Figure S4. As the pulse laser (355 nm) irradiates the photodetectors with pulse duration of 3−5 ns, the loop current increases, leading to an increase of partial voltage on the series resistor. The partial voltage is measured in real-time by the oscilloscope. Figure 3b shows the normalized curve as a function of time. The rise time (the peak photocurrent rises from 10 to 90%) and the decay time (the peak photocurrent decays from 90 to 10%) are estimated to be 0.04 and 2.96 ms for an individual $CsPbBr_3$/CuI device at zero bias, respectively. The high photocurrent, good repeatability, large on/off ratio, and fast speed of the self-powered $CsPbBr_3$/CuI photodetector provide a promising route for developing future photodetectors based on $CsPbBr_3$ single crystals.

The spectral responsivity (R_λ) and detectivity (D^*) are also important parameters to evaluate the performance of self-powered photodetectors. The responsivity is defined as the photocurrent (I_{ph}) per unit of irradiation power, indicating the sensitivity of a detector responding to incident light signals. The detectivity (D^*, typically quoted in Jones) reflects the ability of a detector to detect weak signals from the noise environment. The noise current of a photodetector should comprise all noise sources, but only short noise current is normally considered in the estimation. The responsivity and the detectivity of a photodetector are defined by the following equations:

$$R_\lambda = \frac{I_{ph} - I_d}{P_\lambda S} \tag{1}$$

$$D^* = \frac{R_\lambda}{(2eI_d/S)^{1/2}} \tag{2}$$

DOI: 10.1021/acs.jpclett.9b00960
J. Phys. Chem. Lett. 2019, 10, 2400−2407

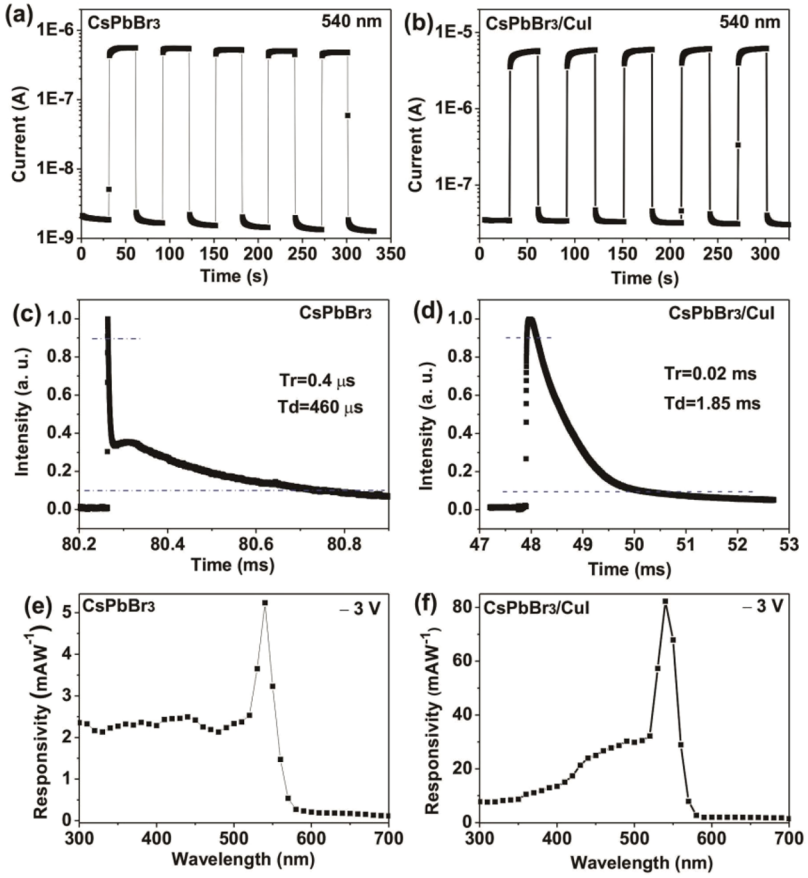

Figure 4. $I-t$ characteristics of (a) $CsPbBr_3$ and (b) $CsPbBr_3$/CuI devices under dark conditions and 540 nm light illumination. Corresponding pulse response of (c) $CsPbBr_3$ and (d) $CsPbBr_3$/CuI devices under 10 Hz 355 nm pulse laser radiation. Spectra responsivity of (e) $CsPbBr_3$ and (f) $CsPbBr_3$/CuI devices with irradiance wavelength ranging from 700 to 300 nm under −3 V bias.

where λ is the irradiation light wavelength, e the electronic charge, I_{ph} the photocurrent, I_d the dark current, P_λ the light power density, and S the effective area under light illumination (measured to be about 0.05 cm^2 in our experiment). The spectral responsivity and detectivity of the $CsPbBr_3$/CuI device with incident wavelength ranging from 700 to 300 nm at zero bias are shown in panels c and d of Figure 3, respectively. The maximum responsivity of the device is 1.4 mA W^{-1} at the wavelength of 540 nm corresponding to the UV−vis absorption spectra of $CsPbBr_3$, which indicates that the device exhibits a high detecting responsivity to signals in the visible region. It is clear that the responsivity increases rapidly from 580 nm (0.1 mA W^{-1}) to 540 nm (1.4 mA W^{-1}) and then decreases dramatically at 520 nm (0.28 mA W^{-1}) in the range of 700−300 nm. As seen in Figure 3c, the sharp cutoff wavelengths defined as the ratio between the maximum and the natural constant ($e \approx 2.718$) appear at 565 and 525 nm, respectively. The detectivity (D^*) has a similar trend as that of the responsivity (R_λ) with a maximum value of 6.2×10^{10} Jones (Figure 3d). The detectivity also shows a narrow detection band at round 540 nm and slowly drops from 500 to 300 nm. These results imply the self-powered $CsPbBr_3$/CuI device has excellent spectral selectivity and is a green-light-sensitive (565−525 nm) photodetector.

To further investigate photoelectric properties, the current−time, response time, and spectra responsivity characteristics of a single $CsPbBr_3$ crystal and individual $CsPbBr_3$/CuI photodetectors were recorded under −3 V bias, and the results are displayed in Figure 4. For the time-resolved photocurrent of the devices under −3 V with the illumination of 540 nm light, they all exhibit a stable and reproducible response (Figure 4a,b). The current of the $CsPbBr_3$ and $CsPbBr_3$/CuI devices rapidly rises to 0.5 and 5 μA, then quickly declines to 1.5 and 30 nA with the light on and off, respectively. The ratios of photocurrent to dark current are calculated to be 320 and 160 under 540 nm light illumination, respectively. Note that the $CsPbBr_3$/CuI device has higher photocurrent than that of the $CsPbBr_3$ device. This result confirms that coating CuI on individual $CsPbBr_3$ crystals can enhance the photocurrent in the visible region. The pure CuI device has high photocurrent and dark current (Figure 2d), but it has a very small on/off ratio and slow speed of response (Figure S5). The formation of a heterojunction is favorable for improving the photocurrent of a $CsPbBr_3$/CuI device. For the response time of the devices, as shown in Figure 4c,d, they all exhibit fast response speed. The rise time from 10% to 90% and the decay time from 90% to 10% of $CsPbBr_3$/CuI devices are 20 μs and 1.85 ms, respectively, which are slightly faster than those at zero bias because of the strengthened built-in electric field. Moreover, the rise time of the $CsPbBr_3$ device is 0.4 μs and the decay time is 0.46 ms, which are much faster than those of the $CsPbBr_3$/CuI device. These results demonstrate that the $CsPbBr_3$ device shows excellent performance, higher photocurrent, and faster speed than that of $CsPbBr_3$ devices previously reported prepared by solution processing methods.[24,26] The $CsPbBr_3$ and $CsPbBr_3$/CuI photodetectors all have good photo-

DOI: 10.1021/acs.jpclett.9b00960
J. Phys. Chem. Lett. 2019, 10, 2400−2407

sensitivity and fast response speed, indicating their potential for developing future microscale photodetectors.

For the wavelength-dependent responsivity of the two devices under −3 V bias, as seen in Figure 4e,f, both $CsPbBr_3$ and $CsPbBr_3$/CuI devices show excellent spectral selectivity. The responsivity peaks of the $CsPbBr_3$ and $CsPbBr_3$/CuI photodetectors are both located at 540 nm, which is the same as that under zero bias, and the responsivities are 5.2 and 82 mA W^{-1}, respectively. Because of enhanced photocurrent, the responsivity of the $CsPbBr_3$/CuI device is much higher than that of the $CsPbBr_3$ device. With the decrease of wavelength (from 700 to 300 nm), the responsivity of the $CsPbBr_3$ photodetector increases rapidly from 0.26 mA W^{-1} (580 nm) to 5.2 mA W^{-1} (540 nm), decreases dramatically to 2.52 mA W^{-1} (520 nm), and fluctuates slightly to 2.35 mA W^{-1} (300 nm). Similarly, the responsivity of the $CsPbBr_3$/CuI device increases quickly from 2.5 mA W^{-1} (580 nm) to 82 mA W^{-1} (540 nm), decreases rapidly to 32 mA W^{-1} (520 nm), and declines stepwise to 7.8 mA W^{-1} (300 nm). In addition, a considerable drop centered at 420 nm corresponds to the band gap of CuI (3.0 eV). Upon light illumination, the pure $CsPbBr_3$ photodetectors exhibit response at 540 nm while $CsPbBr_3$/CuI devices also show high performance upon visible light illumination (540 nm), suggesting that $CsPbBr_3$ plays a key role in the photodetection performance of $CsPbBr_3$/CuI devices. Interestingly, the $CsPbBr_3$ and $CsPbBr_3$/CuI photodetectors showed notable difference in responsivity in the range of 520−300 nm wavelength. The CuI particles deposited on the surface of the $CsPbBr_3$ crystal might have decreased the light penetration distance, and part of the photogenerated charge carriers may be quenched by the holes of CuI under light illumination (<400 nm). Therefore, the corresponding response signals at short wavelength region were further weakened. All these results suggest that the $CsPbBr_3$/CuI photodetector exhibits an enhanced performance and modified responsivity.

According to the Beer−Lambert law, the number of charge carriers in the crystal decreases exponentially with increasing light penetration distance. The high extinction coefficient of $CsPbBr_3$ crystal within the short wavelength indicates a narrow region of photogenerated carriers near the irradiated side, whereas the low extinction coefficient within the long wavelength reveals a broad region. In general, the narrowband photoresponse in the whole spectral range is closely related to the charge diffusion length and light penetration length.[40,41] The charge diffusion length is influenced by the thickness of crystal and the applied bias for photodetectors. Because of the large thickness of the crystal, the $CsPbBr_3$ device exhibits relatively weak response in the short wavelength range. Meanwhile, the surface-charge recombination caused by the light illuminated from the CuI can also decreases the photoresponse. Furthermore, with the decrease of the applied bias, the charge collection efficiency at the electrode will be weakened within short wavelengths. Therefore, the performance of $CsPbBr_3$/CuI narrowband photodetectors based on large-size crystals mainly depends on the thickness of the crystal and the bias applied on devices. For the mechanism of the self-powered $CsPbBr_3$/CuI photodetector, the simplified structure of the device is depicted in Figure 5a. The successful formation of the heterojunction leads to a good rectifying characteristic of the $CsPbBr_3$/CuI device. The photodetector showed high performance around 540 nm, revealing that the $CsPbBr_3$ crystal is the primary carrier transport channel. The

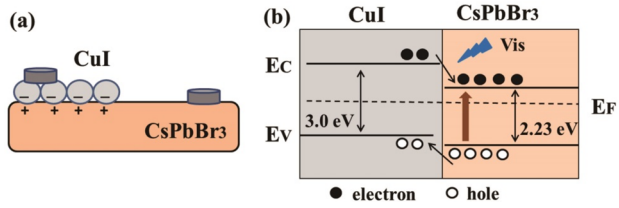

Figure 5. (a) Simplified schematic diagram of photodetector structure. (b) Schematic illustration of energy levels of $CsPbBr_3$/CuI heterojunction and charge-transfer process under 540 nm light illumination.

energy levels of $CsPbBr_3$ and CuI are shown in Figure 5b. The electron affinities of $CsPbBr_3$ and CuI are taken as 2.0 and 3.3 eV,[42,43] and the corresponding band gaps are 2.23 and 3.0 eV, respectively. After surface deposition of the CuI particles, the built-in electric field is formed at the interface and the device presents a type-II heterojunction.[44,45] Under green-light illumination, photogenerated electrons and holes are quickly separated by the built-in field in the depletion layer. The holes will transfer from $CsPbBr_3$ to the valence band of CuI, and the electrons in the conduction band of CuI will drift to the $CsPbBr_3$ to maintain electric neutrality, leading to the formation of photovoltages at the interface yielding a stable photocurrent.[46−49] The device can be considered as a $CsPbBr_3$/CuI p-n heterojunction photodiode. Therefore, the self-powered $CsPbBr_3$/CuI photodetector exhibits high photocurrent, large on/off ratio, fast response speed, and narrowband response. Such filter-free narrowband devices are potentially crucial for a wide range of applications, including imaging, optical communications, machine vision, and many more.

In summary, millimeter-sized $CsPbBr_3$ single crystals were prepared by a facile solvent evaporation method in ambient environment. The $CsPbBr_3$/CuI heterojunction was simply obtained by immersing $CsPbBr_3$ crystals into a CuI solution followed by heat treatment. The device demonstrates a high rectification ratio of 250 at ±2 V. Particularly, the $CsPbBr_3$/CuI photodetector shows high photocurrent (near 100 nA), high photosensitivity (on/off ratio of 1.5×10^3), good wavelength selectivity (565−525 nm), and fast response speed (0.04/2.96 ms) at 540 nm at zero bias. In addition, both $CsPbBr_3$ and $CsPbBr_3$/CuI devices exhibit fast and reproducible responses at 540 nm at −3 V, rise time of 0.4 and 20 μs, decay time of 0.46 and 1.85 ms, respectively, and the latter exhibit significantly increased responsivities. This work provides a simple, low cost, and effective method to prepare millimeter-level $CsPbBr_3$ single crystals. All these promising features reveal that both the pure $CsPbBr_3$ and composite $CsPbBr_3$/CuI devices could be potential candidates for wide practical applications in optoelectronic devices.

EXPERIMENTAL METHODS

Preparation of $CsPbBr_3$ Crystals. All the chemicals were purchased from Aladdin, and the solvents were purchased from Sinopharm. Chemicals were used as received without further purification. First, 0.5 M CsBr (99.9%) and 0.5 M $PbBr_2$ (99.999%) were dissolved in dimethyl sulfoxide (DMSO, 99.9%). The solution was stirred until it was completely dissolved to form a saturated solution and then filtered using a syringe filter. Later, 1 μL of hydroiodic acid solution (55−58 wt %) was added to 10 mL of as-filtered

DOI: 10.1021/acs.jpclett.9b00960
J. Phys. Chem. Lett. 2019, 10, 2400−2407

solution, and the mixture was stirred for 30 min. Subsequently, the solution was transferred to a Petri dish and heated on a heating platform at 40 °C in ambient conditions. With the slow evaporation of DMSO and the prolongation of heating time, the yellow crystals were gradually precipitated. Finally, the large-size $CsPbBr_3$ crystals were carefully washed with isopropanol three times to remove unreacted precursors and dimethyl sulfoxide. Most $CsPbBr_3$ crystals are cuboid in shape, ranging from 4 to 10 mm in length.

Preparation of $CsPbBr_3$/CuI Heterojunction. First, 0.1 M CuI (99.5%) acetonitrile solution was prepared by ultrasonication dissolution. Subsequently, a long $CsPbBr_3$ crystal was selected for device fabrication. Half of the $CsPbBr_3$ crystal was dipped into the as-prepared CuI solution for 1 min. Later the $CsPbBr_3$/CuI heterojunctions were heated at 60 °C in the surrounding environment for 10 min to promote CuI crystallization. Two drops of silver paste were dropped onto the composites as electrodes to construct $CsPbBr_3$/CuI PDs. The diameter of electrodes and channel length are about 0.15 and 0.33 cm, respectively. The active area is about 0.05 cm^2.

Characterization. Field emission scanning electron microscopy (FE-SEM, Zeiss Sigma) was performed to investigate the sample morphologies. Information about the phase of the $CsPbBr_3$ crystals and CuI particles were analyzed using X-ray diffraction (XRD, Bruker D8-A25 diffractometer Cu Kα λ = 1.540 Å, 30 kV, 40 mA) patterns. The elemental composition and their chemical states were examined by X-ray photoelectron spectroscopy (XPS, E PerkinElmer PHI 5000 C ESCA system equipped with a hemispherical electron energy analyzer). The binding energy for C 1s peak at 284.6 eV was used as the reference for calibration. The UV−visible spectra were obtained with a UV−vis spectrophotometer (Hitachi U-3900H) over the range of 200−800 nm. The photoelectric performance of the as-prepared devices was investigated using a program-controlled semiconductor characterization system (Keithley 4200, United States). A NOVA II power meter (OPHIR photonics) was used to measure the light power density. The response speed of the device was measured via the circuit including with a Nd:YAG laser with pulse duration of 3−5 ns (Continuum Electro-Optics, MINILITE II, 355 nm), oscilloscope (Tektronix MSO/DPO5000), and a 10 GΩ resistor. All the measurements were performed in ambient conditions.

■ ASSOCIATED CONTENT

Supporting Information

The Supporting Information is available free of charge on the ACS Publications website at DOI: 10.1021/acs.jpclett.9b00960.

SEM image, XPS spectra, UV−vis absorption spectra, schematic of transient photoresponse measurement system, and *I*−*t* characteristics of CuI (PDF)

■ AUTHOR INFORMATION

Corresponding Author

*E-mail: xshfang@fudan.edu.cn.

ORCID

Xiaosheng Fang: 0000-0003-3387-4532

Notes

The authors declare no competing financial interest.

■ ACKNOWLEDGMENTS

The authors thank Dr. Xiaojie Xu for improvements to the English. This work was supported by Science and Technology Commission of Shanghai Municipality (Grant Nos. 18520744600, 18520710800, and 17520742400), National Postdoctoral Science Foundation of China (2017M621355), National Natural Science Foundation of China (NSFC Grant Nos. 51872050, 11674061, and 11811530065), and Open Project of the State Key Laboratory of Luminescence and Applications (SKLA-2018-05). Part of the research was carried out in Fudan Nanofabrication Laboratory.

■ REFERENCES

(1) Yang, W. S.; Noh, J. H.; Jeon, N. J.; Kim, Y. C.; Ryu, S.; Seo, J.; Seok, S. I. High-performance photovoltaic perovskite layers fabricated through intramolecular exchange. *Science* **2015**, *348*, 1234−1237.

(2) Zhang, Q. P.; Tavakoli, M. M.; Gu, L. L.; Zhang, D. Q.; Tang, L.; Gao, Y.; Guo, J.; Lin, Y. J.; Leung, S. F.; Poddar, S.; Fu, Y.; Fan, Z. Y. Efficient metal halide perovskite light-emitting diodes with significantly improved light extraction on nanophotonic substrates. *Nat. Commun.* **2019**, *10*, 727.

(3) Tong, G.; Li, H.; Li, D.; Zhu, Z.; Xu, E.; Li, G.; Yu, L.; Xu, J.; Jiang, Y. Dual-Phase $CsPbBr_3$-$CsPb_2Br_5$ Perovskite Thin Films via Vapor Deposition for High-Performance Rigid and Flexible Photodetectors. *Small* **2018**, *14*, 1702523.

(4) Lian, X.; Wang, X.; Ling, Y.; Lochner, E.; Tan, L.; Zhou, Y.; Ma, B.; Hanson, K.; Gao, H. Light Emitting Diodes Based on Inorganic Composite Halide Perovskites. *Adv. Funct. Mater.* **2018**, *28*, 1807345.

(5) Belykh, V. V.; Yakovlev, D. R.; Glazov, M. M.; Grigoryev, P. S.; Hussain, M.; Rautert, J.; Dirin, D. N.; Kovalenko, M. V.; Bayer, M. Coherent spin dynamics of electrons and holes in $CsPbBr_3$ perovskite crystals. *Nat. Commun.* **2019**, *10*, 673.

(6) Alarawi, A.; Ramalingam, V.; He, J. H. Recent advances in emerging single atom confined two-dimensional materials for water splitting applications. *Mater. Today Energy* **2019**, *11*, 1−23.

(7) Lin, C. H.; Cheng, B.; Li, T. Y.; Retamal, J. R. D.; Wei, T. C.; Fu, H. C.; Fang, X. S.; He, J. H. Orthogonal Lithography for Halide Perovskite Optoelectronic Nanodevices. *ACS Nano* **2019**, *13*, 1168−1176.

(8) Al-Amri, A. M.; Cheng, B.; He, J. H. Methylammonium Lead Trihalide Perovskite Heterostructures: Progress and Challenges. *IEEE Trans. Nanotechnol.* **2019**, *18*, 1−12.

(9) Xin, B.; Pak, Y.; Mitra, S.; Almalawi, D.; Alwadai, N.; Zhang, Y.; Roqan, I. S. Self-Patterned $CsPbBr_3$ Nanocrystals for High-Performance Optoelectronics. *ACS Appl. Mater. Interfaces* **2019**, *11*, 5223.

(10) Lozano, G. The Role of Metal Halide Perovskites in Next-Generation Lighting Devices. *J. Phys. Chem. Lett.* **2018**, *9*, 3987−3997.

(11) Duan, J.; Zhao, Y.; He, B.; Tang, Q. Simplified perovskite solar cell with 4.1% efficiency employing inorganic $CsPbBr_3$ as light absorber. *Small* **2018**, *14*, 1704443.

(12) Zhao, X.; Liu, T.; Shi, W.; Hou, X.; Dennis, T. J. S. Capillary-written single-crystalline all-inorganic perovskite microribbon arrays for highly-sensitive and thermal-stable photodetectors. *Nanoscale* **2019**, *11*, 2453−2459.

(13) Li, L.; Deng, Y.; Bao, C.; Fang, Y.; Wei, H.; Tang, S.; Zhang, F.; Huang, J. Self-Filtered Narrowband Perovskite Photodetectors with Ultrafast and Tuned Spectral Response. *Adv. Opt. Mater.* **2017**, *5*, 1700672.

(14) Lee, W.; Lee, J.; Yun, H.; Kim, J.; Park, J.; Choi, C.; Kim, D. C.; Seo, H.; Lee, H.; Yu, J. W.; et al. High-Resolution Spin-on-Patterning of Perovskite Thin Films for a Multiplexed Image Sensor Array. *Adv. Mater.* **2017**, *29*, 1702902.

(15) Yang, W.; Hu, K.; Teng, F.; Weng, J. H.; Zhang, Y.; Fang, X. S. High-performance silicon-compatible large-area UV-to-visible broadband photodetector based on integrated lattice-matched type II Se/n-Si heterojunctions. *Nano Lett.* **2018**, *18*, 4697.

DOI: 10.1021/acs.jpclett.9b00960
J. Phys. Chem. Lett. 2019, 10, 2400−2407

(16) Zhang, Z. M.; Ning, Y.; Fang, X. S. From nanofibers to ordered ZnO/NiO heterojunction arrays for self-powered and transparent UV photodetectors. *J. Mater. Chem. C* **2019**, *7*, 223−229.
(17) Zhang, T.; Wang, F.; Zhang, P.; Wang, Y. F.; Chen, H.; Li, J.; Wu, J.; Chen, L.; Chen, Z. D.; Li, S. B. Low-temperature processed inorganic perovskites for flexible detectors with a broadband photoresponse. *Nanoscale* **2019**, *11*, 2871−2877.
(18) Song, J.; Cui, Q.; Li, J.; Xu, J.; Wang, Y.; Xu, L.; Xue, J.; Dong, Y.; Tian, T.; Sun, H.; et al. Ultralarge All-Inorganic Perovskite Bulk Single Crystal for High-Performance Visible-Infrared Dual-Modal Photodetectors. *Adv. Opt. Mater.* **2017**, *5*, 1700157.
(19) Chen, J.; Fu, Y.; Samad, L.; Dang, L.; Zhao, Y.; Shen, S.; Guo, L.; Jin, S. Vapor-phase epitaxial growth of aligned nanowire networks of cesium lead halide perovskites ($CsPbX_3$, X= Cl, Br, I). *Nano Lett.* **2017**, *17*, 460−466.
(20) Ding, J.; Du, S.; Zuo, Z.; Zhao, Y.; Cui, H.; Zhan, X. High Detectivity and rapid response in perovskite $CsPbBr_3$ single-crystal photodetector. *J. Phys. Chem. C* **2017**, *121*, 4917−4923.
(21) Shoaib, M.; Zhang, X.; Wang, X.; Zhou, H.; Xu, T.; Wang, X.; Hu, X.; Liu, H.; Fan, X.; Zheng, W.; et al. Directional growth of ultralong $CsPbBr_3$ perovskite nanowires for high-performance photodetectors. *J. Am. Chem. Soc.* **2017**, *139*, 15592−15595.
(22) Babu, R.; Giribabu, L.; Singh, S. P. Recent Advances in Halide-Based Perovskite Crystals and Their Optoelectronic Applications. *Cryst. Growth Des.* **2018**, *18*, 2645−2664.
(23) Rakita, Y.; Kedem, N.; Gupta, S.; Sadhanala, A.; Kalchenko, V.; Böhm, M. L.; Kulbak, M.; Friend, R. H.; Cahen, D.; Hodes, G. Low-temperature solution-grown $CsPbBr_3$ single crystals and their characterization. *Cryst. Growth Des.* **2016**, *16*, 5717−5725.
(24) Zhang, H.; Liu, X.; Dong, J.; Yu, H.; Zhou, C.; Zhang, B.; Xu, Y.; Jie, W. Centimeter-sized inorganic lead halide perovskite $CsPbBr_3$ crystals grown by an improved solution method. *Cryst. Growth Des.* **2017**, *17*, 6426−6431.
(25) Dirin, D. N.; Cherniukh, I.; Yakunin, S.; Shynkarenko, Y.; Kovalenko, M. V. Solution-grown $CsPbBr_3$ perovskite single crystals for photon detection. *Chem. Mater.* **2016**, *28*, 8470−8474.
(26) Yang, Z.; Xu, Q.; Wang, X.; Lu, J.; Wang, H.; Li, F.; Zhang, L.; Hu, G.; Pan, C. Large and Ultrastable All-Inorganic $CsPbBr_3$ Monocrystalline Films: Low-Temperature Growth and Application for High-Performance Photodetectors. *Adv. Mater.* **2018**, *30*, 1802110.
(27) Saidaminov, M. I.; Haque, M. A.; Almutlaq, J.; Sarmah, S.; Miao, X. H.; Begum, R.; Zhumekenov, A. A.; Dursun, I.; Cho, N.; Murali, B.; et al. Inorganic Lead Halide Perovskite Single Crystals: Phase-Selective Low-Temperature Growth, Carrier Transport Properties, and Self-Powered Photodetection. *Adv. Opt. Mater.* **2017**, *5*, 1600704.
(28) Zhang, Y.; Xu, W. X.; Xu, X. J.; Cai, J.; Yang, W.; Fang, X. S. Self-Powered Dual-Color UV-Green Photodetectors Based on SnO_2 Millimeter Wire and Microwires/$CsPbBr_3$ Particles Heterojunctions. *J. Phys. Chem. Lett.* **2019**, *10*, 836−841.
(29) Zhou, L.; Yu, K.; Yang, F.; Cong, H.; Wang, N.; Zheng, J.; Zuo, Y.; Li, C.; Cheng, B.; Wang, Q. Insight into the effect of ligand-exchange on colloidal $CsPbBr_3$ perovskite quantum dot/mesoporous-TiO_2 composite-based photodetectors: much faster electron injection. *J. Mater. Chem. C* **2017**, *5*, 6224−6233.
(30) Shen, Y.; Wei, C.; Ma, L.; Wang, S.; Wang, X.; Xu, X.; Zeng, H. In situ formation of $CsPbBr_3$/ZnO bulk heterojunctions towards photodetectors with ultrahigh responsivity. *J. Mater. Chem. C* **2018**, *6*, 12164−12169.
(31) Guo, X. B.; Yu, W.; Li, J.; Jiang, Z. Y.; Ma, D. H.; Liu, H. X. Improving microstructure and photoelectric performance of the perovskite material via mixed solvents. *Int. J. Miner., Metall. Mater.* **2017**, *32*, 870−876.
(32) Li, X.; Yu, D.; Chen, J.; Wang, Y.; Cao, F.; Wei, Y.; Wu, Y.; Wang, L.; Zhu, Y.; Sun, Z.; et al. Constructing fast carrier tracks into flexible perovskite photodetectors to greatly improve responsivity. *ACS Nano* **2017**, *11*, 2015−2023.
(33) Teng, F.; Hu, K.; Ouyang, W.; Fang, X. S. Photoelectric Detectors Based on Inorganic p-Type Semiconductor Materials. *Adv. Mater.* **2018**, *30*, 1706262.
(34) Ji, Y.; Yang, J.; Luo, W.; Tang, L.; Bai, X.; Leng, C.; Ma, C.; Wei, X.; Wang, J.; Shen, J.; et al. Ultraflexible and High-Performance Multilayer Transparent Electrode Based on ZnO/Ag/CuSCN. *ACS Appl. Mater. Interfaces* **2018**, *10*, 9571−9578.
(35) He, Y.; Fishman, Z. S.; Yang, K. R.; Ortiz, B.; Liu, C.; Goldsamt, J.; Batista, V. S.; Pfefferle, L. D. Hydrophobic CuO Nanosheets Functionalized with Organic Adsorbates. *J. Am. Chem. Soc.* **2018**, *140*, 1824−1833.
(36) Sun, W.; Ye, S.; Rao, H.; Li, Y.; Liu, Z.; Xiao, L.; Chen, Z.; Bian, Z.; Huang, C. Room-temperature and solution-processed copper iodide as the hole transport layer for inverted planar perovskite solar cells. *Nanoscale* **2016**, *8*, 15954−15960.
(37) Christians, J. A.; Fung, R. C.; Kamat, P. V. An inorganic hole conductor for organo-lead halide perovskite solar cells. Improved hole conductivity with copper iodide. *J. Am. Chem. Soc.* **2014**, *136*, 758−764.
(38) Liu, C.; Peng, M.; Yu, A.; Liu, J.; Song, M.; Zhang, Y.; Zhai, J. Interface engineering on p-CuI/n-ZnO heterojunction for enhancing piezoelectric and piezo-phototronic performance. *Nano Energy* **2016**, *26*, 417−424.
(39) Yang, C.; Kneiß, M.; Schein, F.-L.; Lorenz, M.; Grundmann, M. Room-temperature domain-epitaxy of copper iodide thin films for transparent CuI/ZnO heterojunctions with high rectification ratios larger than 109. *Sci. Rep.* **2016**, *6*, 21937.
(40) Fang, Y.; Dong, Q.; Shao, Y.; Yuan, Y.; Huang, J. Highly narrowband perovskite single-crystal photodetectors enabled by surface-charge recombination. *Nat. Photonics* **2015**, *9*, 679.
(41) Rao, H. S.; Li, W. G.; Chen, B. X.; Kuang, D. B.; Su, C. Y. In Situ Growth of 120 cm^2 CH3NH3PbBr$_3$ Perovskite Crystal Film on FTO Glass for Narrowband-Photodetectors. *Adv. Mater.* **2017**, *29*, 1602639.
(42) Li, Y.; Shi, Z.; Lei, L.; Zhang, F.; Ma, Z.; Wu, D.; Xu, T.; Tian, Y.; Zhang, Y.; Du, G.; et al. Highly Stable Perovskite Photodetector Based on Vapor-Processed Micrometer-Scale $CsPbBr_3$ Microplatelets. *Chem. Mater.* **2018**, *30*, 6744−6755.
(43) Yamada, N.; Ino, R.; Ninomiya, Y. Truly transparent p-type γ-CuI thin films with high hole mobility. *Chem. Mater.* **2016**, *28*, 4971−4981.
(44) Ouyang, W. X.; Teng, F.; Fang, X. S. High Performance BiOCl Nanosheets/TiO_2 Nanotube Arrays Heterojunction UV Photodetector: The Influences of Self-Induced Inner Electric Fields in the BiOCl Nanosheets. *Adv. Funct. Mater.* **2018**, *28*, 1707178.
(45) Ouyang, W. X.; Teng, F.; He, J. H.; Fang, X. S. Enhancing the Photoelectric Performance of Photodetectors Based on Metal Oxide Semiconductors by Charge-Carrier Engineering. *Adv. Funct. Mater.* **2019**, *29*, 1807672.
(46) Alarawi, A.; Ramalingam, V.; Fu, H. C.; Varadhan, P.; Yang, R. S.; He, J. H. Enhanced photoelectrochemical hydrogen production efficiency of MoS_2-Si heterojunction. *Opt. Express* **2019**, *27*, A352−A362.
(47) Gao, N.; Fang, X. S. Synthesis and Development of Graphene−Inorganic Semiconductor Nanocomposites. *Chem. Rev.* **2015**, *115*, 8294−8343.
(48) Liu, S. X.; Zheng, L. X.; Yu, P. P.; Han, S. C.; Fang, X. S. Novel Composites of α-Fe_2O_3 Tetrakaidecahedron and Graphene Oxide as an Effective Photoelectrode with Enhanced Photocurrent Performances. *Adv. Funct. Mater.* **2016**, *26*, 3331−3339.
(49) Bullock, J.; Amani, M.; Cho, J.; Chen, Y. Z.; Ahn, G. H.; Adinolfi, V.; Shrestha, V. R.; Gao, Y.; Crozier, K. B.; Chueh, Y. L.; Javey, A. Polarization-resolved black phosphorus/molybdenum disulfide mid-wave infrared photodiodes with high detectivity at room temperature. *Nat. Photonics* **2018**, *12*, 601−607.

DOI: 10.1021/acs.jpclett.9b00960
J. Phys. Chem. Lett. 2019, 10, 2400−2407